J. Fluid Mech. (2008), *vol.* 615, *pp.* 185–210.
doi:10.1017/S0022112008003467 Printed in the United Kingdom

Channel formation by turbidity currents: Navier–Stokes-based linear stability analysis

B. HALL[1], E. MEIBURG[1]† AND B. KNELLER[2]

[1]Department of Mechanical Engineering, University of California, Santa Barbara, CA 93106, USA
[2]Department of Geology and Petroleum Geology, University of Aberdeen, Aberdeen AB24 3FX, UK

(Received 10 October 2007 and in revised form 14 July 2008)

The linear stability of an erodible sediment bed beneath a turbidity current is analysed, in order to identify potential mechanisms responsible for the formation of longitudinal gullies and channels. On the basis of the three-dimensional Navier–Stokes equations, the stability analysis accounts for the coupled interaction of the three-dimensional fluid and particle motion inside the current with the erodible bed below it. For instability to occur, the suspended sediment concentration of the base flow needs to decay away from the sediment bed more slowly than does the shear stress inside the current. Under such conditions, an upward protrusion of the sediment bed will find itself in an environment where erosion decays more quickly than sedimentation, and so it will keep increasing. Conversely, a local valley in the sediment bed will see erosion increase more strongly than sedimentation, which again will amplify the initial perturbation.

The destabilizing effect of the base flow is modulated by the stabilizing perturbation of the suspended sediment concentration and by the shear stress due to a secondary flow structure in the form of counter-rotating streamwise vortices. These streamwise vortices are stabilizing for small Reynolds and Péclet numbers and destabilizing for large values.

For a representative current height of $O(10–100\,\mathrm{m})$, the linear stability analysis provides the most amplified wavelength in the range of 250–2500 m, which is consistent with field observations reported in the literature. In contrast to previous analyses based on depth-averaged equations, the instability mechanism identified here does not require any assumptions about sub- or supercritical flow, nor does it require the presence of a slope or a slope break.

1. Introduction

Submarine channels and gullies play an important role as pathways for sediment transport across continental shelves and down continental slopes. They range in width from $O(100\,\mathrm{m})$ to several kilometres, and from a few metres to hundreds of metres deep. Since they contribute significantly to the architecture of slope deposits (Syvitski *et al.* 1996), it is desirable to obtain insight into the processes underlying their formation. While a clear understanding of the governing mechanisms and their interplay has not yet evolved, both erosion by turbidity currents and deposition from the overlying water column are believed to play a role in their formation (Field, Gardner & Prior 1999; cf. also Campbell *et al.* 2004). Interestingly,

† Author to whom correspondence should be addressed: meiburg@engineering.ucsb.edu

as these authors point out, gullies and channels on the sea floor frequently appear in straight evenly spaced patterns, which suggest the presence of an underlying coupled hydrodynamic/sediment-driven instability.

The hypothesis of an instability mechanism at the heart of submarine and subaerial channel inception has spawned a number of investigations, based on a variety of flow and sediment transport models, starting with the work of Smith & Bretherton (1972). Izumi & Parker (1995) considered the generation of terrestrial channel systems as a result of shallow overland flow due to rainfall. By employing a set of depth-averaged flow equations in conjunction with the Exner equation for the sediment bed, they showed that the presence of a threshold condition for bed erosion provides a wavelength selection criterion that predicts the correct order of magnitude. Since a sufficiently strong base flow due to rainfall is needed to cause erosion, they termed their theory 'upstream-driven'. The extension to non-flat sediment beds was undertaken by Revelli & Ridolfi (2000). A complementary 'downstream-driven' theory was presented by Izumi & Parker (2000) for a downward-concave hillslope, along which a base state slowly migrates in the upstream direction. Birnir, Smith & Merchant (2001) employed deterministic and stochastic elements in analysing the processes underlying river basin formation. For their system of depth-averaged equations, white noise is seen to give rise to a channelization process that reproduces several of the scaling laws observed in nature.

The case of channel inception by submarine sediment gravity flows was addressed by Imran, Parker & Katopodes (1998). These authors analysed the role of erosional and depositional turbidity currents, based on initial-value simulations of the depth-averaged equations. A key hypothesis in their argument lies in the assumption that the erosion rate has a narrower peak in the transverse direction than the deposition rate. While their model provides insight into the formation of a single channel downstream of a submarine canyon, it does not address the generation of equidistantly spaced parallel arrays of channels. Similarly, the depth-averaged numerical simulations by Fedele (2003) exhibit channel-like topographical features that develop preferentially in the presence of a slope break.

Building on the 'downstream-driven' theory of Izumi & Parker (2000), Izumi (2004) conducted a linear stability investigation into the formation of submarine gullies by turbidity currents (cf. also the investigation by Izumi & Fujii 2006). Again, layer-averaged equations were employed for a spatially developing downward-concave slope profile. The author obtained an estimate of the preferred wavelength in the range of 150–8000 m, which is consistent with field observations. A physical explanation for the observed instability is not presented.

All of these investigations are based on depth-averaged equations, and consequently they do not provide any insight into the transverse flow structure near the sediment bed. Specifically, potential coupling mechanisms between the spanwise and vertical velocity components on one hand and the erosion process on the other cannot be explored with this approach. A hint that such coupling mechanisms may be important with regard to the formation of longitudinal topographical features is found in the investigation by Colombini (1993), who draws attention to the importance of secondary transverse flow structures in the form of counter-rotating streamwise vortices. The author formulates a stability problem for the sediment that invokes a turbulence closure model resulting in the formation of secondary streamwise vortices. This flow causes spanwise bedload transport, which deforms the geometry of the sediment bed, and thus causes a feedback onto the fluid velocity field. This approach yields an eigenvalue problem for the stability of the sediment bed which indicates

a competition between the destabilizing secondary flow and the stabilizing effects of gravity. A related experimental investigation was conducted by Wang & Cheng (2005). Colombini & Parker (1995) further elaborated on this concept with a view towards generating small amplitude 'streak' features of a few grain diameters. Further connections between the structural elements of turbulent boundary-layer flows and topographical features of sediment beds are reviewed in the papers by Blondeaux (2001) and Gyr & Kinzelbach (2004).

In contrast to these studies, the present investigation aims to explore the importance of two-way coupling mechanisms between transverse flow structures and suspended sediment for the formation of submarine gullies and channels. Towards this end, we conduct a linear stability analysis based on the full Navier–Stokes equations rather than depth-averaged equations. The base flow around which the equations will be linearized mimics a turbidity current propagating over a nominally plane sediment bed. For an introduction to the rich topic of gravity and turbidity currents, the reader is referred to the monograph by Simpson (1997). Submarine turbidity currents can be maintained for extended periods of time, and so they can give rise to well-developed and approximately quasi-steady flow fields that are suitable as a basis for conducting a linear stability investigation. Typically, turbidity currents are characterized by pronounced vertical profiles of the suspended particle concentration and the streamwise velocity above the sediment bed (cf. Parker *et al.* 1987; Stacey & Bowen 1988; Chikita 1990; Garcia & Parker 1993; Garcia 1994; Altinakar, Graf & Hopfinger 1996; Kneller & Buckee 2000; McCaffrey *et al.* 2003; Choux *et al.* 2005). These vertical profiles, and their interaction with the sediment bed, will represent the focus of our investigation.

The flow model will be introduced in § 2, along with the governing equations and the corresponding dimensionless parameters. These equations will be linearized around the unidirectional quasi-steady base state, thus resulting in a computational eigenvalue problem that can be solved numerically. Section 3 presents solutions in the form of dispersion relations and eigenfunctions, whose detailed analysis provides insight into the governing physical mechanisms. The key conclusions will be presented in § 4.

2. Model formulation

2.1. *Governing equations*

The mathematical description of the turbidity current flow field follows the approach introduced by Necker *et al.* (2002, 2005). It employs the three-dimensional incompressible Navier–Stokes equations in the Boussinesq approximation, based on the assumption of moderate density variations. We assume that the suspended particle concentration is sufficiently small for the fluid–particle interactions to occur primarily through the momentum equations, and for the effect of the particles in the continuity equation to be negligible (Necker *et al.* 2005). A convection–diffusion equation accounts for the motion of the particulate phase. We consider small monodisperse particles with negligible inertia, whose velocity equals the sum of the fluid velocity plus a constant downward-settling velocity w_s. Note that this modelling approach is appropriate for turbidity currents, but would not be applicable to, say, debris flows. The analysis focuses on a cross-section of the flow, as shown in figure 1, where the flow is fully developed in the streamwise x-direction ($\partial/\partial x = 0$, except for the pressure).

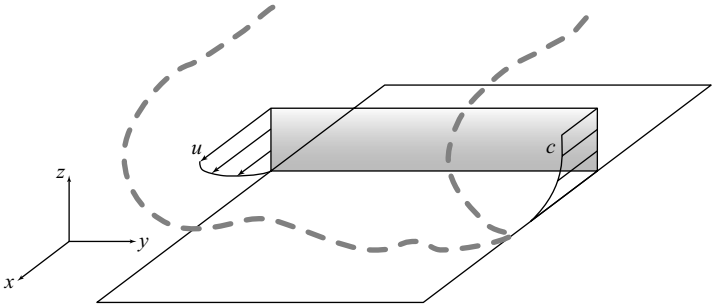

FIGURE 1. The linear stability analysis focuses on the current–substrate boundary layer in a cross-section of the turbidity current. This cross-section is located some distance behind the current head, where the flow is well developed.

Hence we obtain the two-dimensional three-component system

$$\frac{\partial v}{\partial y} + \frac{\partial w}{\partial z} = 0, \tag{2.1}$$

$$\frac{\partial u}{\partial t} + v\frac{\partial u}{\partial y} + w\frac{\partial u}{\partial z} = -\frac{1}{\rho_f}\frac{\partial p}{\partial x} + \nu\left(\frac{\partial^2 u}{\partial y^2} + \frac{\partial^2 u}{\partial z^2}\right), \tag{2.2}$$

$$\frac{\partial v}{\partial t} + v\frac{\partial v}{\partial y} + w\frac{\partial v}{\partial z} = -\frac{1}{\rho_f}\frac{\partial p}{\partial y} + \nu\left(\frac{\partial^2 v}{\partial y^2} + \frac{\partial^2 v}{\partial z^2}\right), \tag{2.3}$$

$$\frac{\partial w}{\partial t} + v\frac{\partial w}{\partial y} + w\frac{\partial w}{\partial z} = -\frac{1}{\rho_f}\frac{\partial p}{\partial z} + \nu\left(\frac{\partial^2 w}{\partial y^2} + \frac{\partial^2 w}{\partial z^2}\right) - \frac{\rho}{\rho_f}g, \tag{2.4}$$

$$\frac{\partial c}{\partial t} + v\frac{\partial c}{\partial y} + (w - w_s)\frac{\partial c}{\partial z} = D\left(\frac{\partial^2 c}{\partial y^2} + \frac{\partial^2 c}{\partial z^2}\right). \tag{2.5}$$

Here, u, v and w denote the components of the velocity vector. ν represents the (constant) eddy viscosity of the flow and D indicates an effective turbulent diffusion coefficient for the particulate phase. We note that a real turbidity current will not have a constant eddy viscosity (Stacey & Bowen 1988). However, we do not know the precise form of the turbulent stress tensor in a complex flow such as the present one (variable concentration, particle-laden flow near an erodible sediment bed). Hence we feel it is best to employ the simplest possible turbulence model in the form of a constant eddy viscosity. As we will see later, this approach is adequate for capturing the basic instability mechanism.

We refer (2.1)–(2.5) as the Navier–Stokes equations, even though ν and D represent effective turbulent transport properties rather than molecular quantities. The density ρ of the suspension is linearly related to the volume fraction c of the particles by $\rho(c) = \rho_f(1 + \gamma c)$, where $\rho_f(\rho_p)$ is the fluid (particle) density and $\gamma = (\rho_p - \rho_f)/\rho_f$ represents the excess density ratio. Note that, in employing these systems of equations, we assume the interactions among particles to be small, and so effects such as hindered settling or an increase in the effective viscosity of the suspension can be safely neglected.

To analyse the coupled dynamics of the turbidity current and the fluid–substrate interface, we require an equation that describes how the interface location changes as a result of particle settling and erosion. Towards this end, we define the interface position by its height $\eta(y, t)$ above the y-axis (cf. figure 2). Now, we will separately discuss the effects of particle settling and erosion.

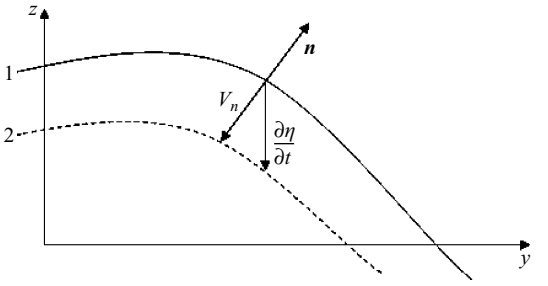

FIGURE 2. As a result of particle sedimentation and erosion, the interface location $\eta(y, t)$ evolves as a function of time.

Particle settling: The rate at which the interface moves upward due to particle sedimentation is given by the settling velocity and the particle volume fraction at the interface according to

$$\frac{\partial \eta}{\partial t} = w_s c(z = \eta). \tag{2.6}$$

Note that we neglect the volume of the interstitial voids in the sediment bed. In order to account for this effect, we would have to assume a packing ratio, which in turn has to be based on assuming a certain grain shape. This packing ratio would multiply the left-hand side of the equation, indicating a faster advancement of the interface. However, as will be seen later, the effect of the packing ratio is not essential to the linear instability mechanism that will be identified. Consequently, as a first approximation, we neglect its influence.

Particle erosion: The erosion of particles from the interface causes the interface to recede in the direction normal to itself, as sketched in figure 2. This shows an interface that is receding from position 1 to position 2 with time. The erosion velocity V_n is the rate at which the interface recedes in the direction normal to itself. This direction is defined by the unit vector

$$\boldsymbol{n} = \frac{1}{\sqrt{1 + (\partial \eta/\partial y)^2}} \begin{pmatrix} \partial \eta/\partial y \\ 1 \end{pmatrix}. \tag{2.7}$$

The rate of change $\partial \eta/\partial t$ in the interface height is related to the erosion velocity by

$$\frac{\partial \eta}{\partial t} = -\frac{|V_n|}{n_z}. \tag{2.8}$$

On the basis of a series of flume experiments, Garcia & Parker (1993) established a relationship among the erosional particle flux, the shear stress at the fluid–substrate interface, the particle Reynolds number and the settling velocity. They observe a threshold-like behaviour, which reflects a sudden onset, increase and saturation of erosion over a relatively small interval in the parameter regime. Such threshold-like behaviour is always nonlinear and cannot be incorporated into a linear stability analysis. Hence, for the purpose of the present stability analysis, we replace the threshold-like behaviour with a linear relationship between the erosional particle flux and the shear stress at the fluid–substrate interface

$$|V_n| = \beta \tau_n. \tag{2.9}$$

Here again, if we account for the interstitial void fraction, the packing ratio would multiply the left-hand side. The constant β quantifies the rate at which particle volume is eroded per unit area and per unit shear stress. It depends on factors such as particle size, shape and cohesion and is measured in $\mathrm{m^2\,s\,kg^{-1}}$. While this linearization of the experimentally observed threshold behaviour represents an idealization, it will nevertheless allow us to gain insight into the physical mechanisms governing the instability of the fluid–substrate interface. The results will have to be interpreted correspondingly. Clearly, if the flow is such that the shear stress at the surface of the sediment bed is below the threshold for erosion everywhere, an instability will not be observed.

The experiments by Garcia & Parker (1993) provide information regarding the rate at which particle volume is eroded from the interface as a function of the flow and particle parameters. However, it is not entirely clear how the nature of the particle transport away from the interface can be described mathematically. For the purpose of the present analysis, we assume that the motion of the particles away from the interface is primarily caused by the turbulent eddies of the flow rather than by particle collisions or other processes. Hence we model this particle transport away from the interface as a (turbulent) diffusive flux, following the approach of other authors (Parker 1978; Blanchette *et al.* 2005):

$$D\left.\frac{\partial c}{\partial n}\right|_{z=\eta} = -\beta\tau_n. \tag{2.10}$$

Note that the issue of modelling the particle flux away from the sediment bed does not arise within the framework of depth-averaged equations. In such an approach, vertical fluxes are assumed to be negligible, and erosion is accounted for by distributing particles instantaneously in a uniform fashion across the entire height of the current. Combining (2.8) with (2.9) provides a relation for the evolution of the interface height due to erosion in the form

$$\frac{\partial \eta}{\partial t} = -\beta\frac{\tau_n}{n_z}. \tag{2.11}$$

By superimposing the depositional (2.6) and erosional (2.11) components, we thus obtain the following evolution equation for the interface height:

$$\frac{\partial \eta}{\partial t} = w_s c(z=\eta) - \beta\frac{\tau_n}{n_z}. \tag{2.12}$$

Equations (2.1), (2.5) and (2.12) comprise the evolution equations for the coupled turbidity current–substrate dynamics in terms of u, v, w, p, c and η. At the interface, no-slip conditions are imposed for the u- and v-velocity components, while the w-velocity component has to equal the rate at which the interface advances or recedes in the vertical direction

$$u(z=\eta) = 0, \tag{2.13}$$

$$v(z=\eta) = 0, \tag{2.14}$$

$$w(z=\eta) = \frac{\partial \eta}{\partial t}. \tag{2.15}$$

If the interstitial void fraction was to be accounted for, the packing ratio would multiply the right-hand side of the boundary condition for w. Since the present work focuses on instability mechanisms in systems governed by the Navier–Stokes

equations, note that we avoid effective slip conditions such as the one introduced by Engelund (1964).

2.2. *Non-dimensionalization*

In order to render the above system of equations and boundary conditions dimensionless, we introduce $l^* = D/w_s$ as the characteristic length scale. l^* represents a measure of the particle concentration boundary-layer thickness which, to a first degree, is governed by a balance of downward settling and upward (turbulent) diffusion. Note that the assumption of a balance between settling and diffusion represents a relatively crude approximation of the mechanisms governing particle settling in turbulent shear flows. It is well known that both one-way and two-way coupling effects exist in such flows that modify the settling motion of particles. Detailed investigations of these mechanisms have shown both delayed (Raju & Meiburg 1995) and accelerated (Bosse, Kleiser & Meiburg 2006) settling.

Together with the typical streamwise velocity $u^* = u_\infty$ in the main body of the current, the above scaling yields as characteristic time $t^* = l^*/u^* = D/(w_s u_\infty)$. Pressure is scaled with $p^* = \rho_f (u^*)^2$, and a characteristic shear stress is obtained as $\tau^* = u^* \nu \rho_f / l^*$. The value c_∞ in the body of the current is taken as the characteristic concentration c^*. For dilute turbidity currents, we can assume $c^* \leqslant O(10^{-2})$. As characteristic density difference ρ^*, we employ $c_\infty(\rho_p - \rho_f)$, i.e. the excess density due to particle loading in the body of the turbidity current. u_∞ and c_∞ will be further discussed later in the context of the unidirectional base flow.

It is important to realize that the formation of channels may take place during net overall deposition or erosion (Field *et al.* 1999), i.e. an overall upward or downward motion of the interface. Since the linear stability analysis is to be performed for a quasi-steady base state, we shift to a reference frame that moves with the velocity of the advancing–receding interface. If the unperturbed interface moves with a dimensionless velocity $\mathrm{d}\eta/\mathrm{d}t = w_{av}$ in the laboratory reference frame, we introduce $z' = z - w_{av}t$, $\eta' = \eta - w_{av}t$ and $w' = (w - w_{av})$. After shifting into this new reference frame, and omitting the primes, the set of governing field equations remains unchanged, and we obtain

$$\frac{\partial v}{\partial y} + \frac{\partial w}{\partial z} = 0, \tag{2.16}$$

$$\frac{\partial u}{\partial t} + v\frac{\partial u}{\partial y} + w\frac{\partial u}{\partial z} = -\frac{\partial p}{\partial x} + \frac{1}{Re}\left(\frac{\partial^2 u}{\partial y^2} + \frac{\partial^2 u}{\partial z^2}\right), \tag{2.17}$$

$$\frac{\partial v}{\partial t} + v\frac{\partial v}{\partial y} + w\frac{\partial v}{\partial z} = -\frac{\partial p}{\partial y} + \frac{1}{Re}\left(\frac{\partial^2 v}{\partial y^2} + \frac{\partial^2 v}{\partial z^2}\right), \tag{2.18}$$

$$\frac{\partial w}{\partial t} + v\frac{\partial w}{\partial y} + w\frac{\partial w}{\partial z} = -\frac{\partial p}{\partial z} + \frac{1}{Re}\left(\frac{\partial^2 w}{\partial y^2} + \frac{\partial^2 w}{\partial z^2}\right) - Gc, \tag{2.19}$$

$$\frac{\partial c}{\partial t} + v\frac{\partial c}{\partial y} + \left(w - \frac{1}{Pe}\right)\frac{\partial c}{\partial z} = \frac{1}{Pe}\left(\frac{\partial^2 c}{\partial y^2} + \frac{\partial^2 c}{\partial z^2}\right), \tag{2.20}$$

$$\frac{\partial \eta}{\partial t} = -w_{av} + \frac{c_\infty}{Pe}c(z = \eta) - N\frac{\tau_n}{n_z}. \tag{2.21}$$

Here the Reynolds number, based on the thickness of the concentration boundary layer as the characteristic length scale, is defined as $Re = u_\infty D/\nu w_s$. The Péclet number $Pe = u_\infty/w_s$ represents the ratio of the characteristic streamwise velocity of the current to the settling velocity. Alternatively, Pe indicates an inverse dimensionless diffusion coefficient. It can be interpreted as the ratio of two time scales, viz. the time it takes

for a particle to diffuse across the concentration boundary layer versus the time it would take a particle moving with u_∞ to cover the same distance. It is to be kept in mind that D indicates an effective turbulent diffusion coefficient for the particle transport, while ν represents an effective turbulent diffusion coefficient for momentum. For small particles, we can assume D and ν to be roughly of the same magnitude, and so we will often employ $Re = Pe$ in the following.

The gravitational parameter, $G = (c_\infty(\rho_p - \rho_f)gD)/(\rho_f u_\infty^2 w_s)$ represents the ratio of gravitational to inertial forces. The erosion coefficient $N = \beta\nu\rho_f w_s/D$ describes the ratio of the velocity at which the interface recedes as a result of erosion and of the free stream velocity. The dimensionless boundary conditions become

$$u(z = \eta) = 0, \tag{2.22}$$

$$v(z = \eta) = 0, \tag{2.23}$$

$$w(z = \eta) = \frac{\partial \eta}{\partial t}, \tag{2.24}$$

$$\left.\frac{\partial c}{\partial n}\right|_{z=\eta} = -\frac{NPe}{c_\infty}\tau_n. \tag{2.25}$$

In order to associate meaningful numerical values with the above dimensionless parameters, it is helpful to employ typical orders of magnitude for the involved quantities. Settling velocities of sand grains commonly are in the range of a few tens of millimetres per second. Laboratory and environmental measurements of turbidity currents (Parker *et al.* 1987; Chikita 1989; Normark 1989; Chikita 1990; Garcia 1994; Altinakar *et al.* 1996; McCaffrey *et al.* 2003; Choux *et al.* 2005) indicate that the concentration of suspended particles decays fairly uniformly across the entire height of the current, and so a characteristic 'decay length' should be of the same order of magnitude as the current height. Hence a representative value of l^* may be in the range of 10–100 m (Komar 1969; Zeng *et al.* 1991; Piper & Savoye 1993). These values yield an effective turbulent diffusion coefficient in the range of 0.1–1 $\mathrm{m^2\,s^{-1}}$. A characteristic streamwise velocity of the current is 10 $\mathrm{m\,s^{-1}}$, and so we obtain a typical value of $Pe = Re \approx 10^3$. For $(\rho_p - \rho_f)/\rho_f \approx 1$, the preceding estimates yield $G \approx$ 0.1–1. As discussed earlier, the assumption of a linear relationship between the erosion rate and the shear stress at the surface of the sediment bed represents a relatively crude approximation of the more threshold-like behaviour observed experimentally by Garcia & Parker (1993). While the relationship forwarded by these authors does not allow us to determine a representative value for β, we can nevertheless safely assume that $N \leqslant O(10^{-5})$.

2.3. *Unidirectional quasi-steady base state*

We address the situation of a turbidity current flowing into ambient clear fluid at rest. The linear stability analysis focuses on a cross-section of the turbidity current some distance behind the head, where the flow is well developed and changes slowly in the x-direction (except for the pressure). We derive a unidirectional one-dimensional quasi-steady base state by assuming

$$\frac{\partial}{\partial t} = \frac{\partial}{\partial x} = \frac{\partial}{\partial y} \equiv 0, \tag{2.26}$$

$$v = w \equiv 0. \tag{2.27}$$

We note that assuming $\partial/\partial x = 0$ represents a simplification of real currents, which typically evolve in the streamwise direction due to entrainment. As we will see, this

assumption still allows us to develop a realistic model of a base state that retains all of the characteristic features of real currents required for a linear instability to develop. We obtain for the base state variables $u_o(z)$, $p_o(x, z)$ and $c_o(z)$ and for the velocity w_{av} at which the interface rises/recedes

$$\frac{\partial p_o}{\partial x} = \frac{1}{Re}\frac{\mathrm{d}^2 u_o}{\mathrm{d}z^2}, \tag{2.28}$$

$$\frac{\partial p_o}{\partial z} = -Gc_o, \tag{2.29}$$

$$\frac{\mathrm{d}c_o}{\mathrm{d}z} = -\frac{\mathrm{d}^2 c_o}{\mathrm{d}z^2}, \tag{2.30}$$

$$w_{av} = \frac{c_\infty}{Pe}c_o(z=0) - N\left.\frac{\mathrm{d}u_o}{\mathrm{d}z}\right|_{z=0}. \tag{2.31}$$

We assume that the instability giving rise to the formation of channels and gullies is governed by the interaction of the sediment bed with the regions of the current immediately above, where the velocity increases and the sediment concentration decreases. The results of the analysis will confirm the validity of this assumption a posteriori, as they will show that the vertical extent of the eigenfunctions is limited to the flow regions near the sediment bed. Consequently, the features of the base flow profile beyond this nearwall region will not affect the linear stability results. Hence we can apply as boundary conditions

$$u_o(z=0) = 0, \tag{2.32}$$

$$u_o(z\to\infty) = 1, \tag{2.33}$$

$$\left.\frac{\mathrm{d}c_o}{\mathrm{d}z}\right|_{z=0} = -\frac{NPe}{c_\infty}\left.\frac{\mathrm{d}u_o}{\mathrm{d}z}\right|_{z=0}, \tag{2.34}$$

$$c_o(z\to\infty) = 1. \tag{2.35}$$

In principle, it would be possible to employ base flow models for the velocity and concentration that capture the presence of the clear ambient fluid at rest above the current. While this would not affect the analysis of the channelization instability, it would likely capture the Kelvin–Helmholtz and Holmboe instabilities of the mixing layer separating the turbidity current from the ambient fluid above. Since the analysis of these instabilities is beyond the scope of the current work, and so we limit the present analysis to the near-wall region.

By using (2.30) and applying boundary conditions (2.34) and (2.35), we obtain

$$c_o(z) = \frac{NPe}{c_\infty}\left.\frac{\mathrm{d}u_o}{\mathrm{d}z}\right|_{z=0}\mathrm{e}^{-z} + 1. \tag{2.36}$$

To obtain the base flow velocity profile $u_o(z)$, we need information on the base pressure profile $p_o(x, z)$. Since the base concentration profile varies exponentially with z in the boundary layer, we assume that p_o also varies exponentially with z. However, we allow for the fact that this variation may occur over a different length scale $L \neq 1$, and so the velocity and concentration boundary layers may have different thicknesses. We also assume that the pressure variation in the x-direction is separable from the variation in the z-direction

$$p_o(x, z) = A(x)\mathrm{e}^{-z/L}. \tag{2.37}$$

Note that an arbitrary function $F(z)$ can be added to the base pressure in (2.37) in order to obtain any desired far field decay. This arbitrary function $F(z)$ will not affect the linear stability analysis.

Thus from (2.28) and (2.37) we obtain

$$\frac{\mathrm{d}^2 u_o}{\mathrm{d}z^2} = A'(x)\mathrm{e}^{-z/L}. \tag{2.38}$$

Integrating twice and applying the boundary conditions (2.32) and (2.33) gives

$$u_o(z) = 1 - \mathrm{e}^{-z/L}. \tag{2.39}$$

In turn, this yields for the concentration profile

$$c_o(z) = \frac{NPe}{Lc_\infty}\,\mathrm{e}^{-z} + 1. \tag{2.40}$$

Equations (2.39) and (2.40) represent the base flow profile around which the governing equations will be linearized. The dimensionless base flow shear stress at the interface can be determined by differentiating (2.39) to give $1/L$. Thus N/L is a measure of erosion at the interface, while c_∞/Pe represents the importance of interface growth due to sedimentation. Consequently, the dimensionless parameter group in (2.40) denotes the ratio of settling and erosion near the interface.

Note that the balance between settling and erosion described by eqn. (2.31) determines the quasi-steady velocity w_{av} with which the surface of the sediment bed advances upward for the base state. For the base state described earlier, it yields $w_{av} = c_\infty/Pe$. This reflects the fact that for a quasi-steady base state, there is no accumulation of particles in the concentration boundary layer. Hence the rate at which particles sediment out at the bottom equals the rate at which particles enter the boundary layer from above, which is given by c_∞/Pe, with Pe denoting the dimensionless inverse settling velocity. Note that the quasi-steady base state describes a current with net deposition. For an eroding current, particles would enter the base flow both from below (through erosion from the bed) and from above (through sedimentation from the core of the turbidity current), and so there would be a continuous accumulation of particles in the near-wall region. This would have to be modelled via an unsteady base flow. We remark that from a physical point of view, the assumption of different velocity and concentration boundary-layer thicknesses is reasonable and in agreement with laboratory observations (Parker *et al.* 1987; Garcia 1994; Altinakar *et al.* 1996; McCaffrey *et al.* 2003; Choux *et al.* 2005). While the velocity boundary-layer thickness is governed primarily by the Reynolds number Re, the concentration boundary-layer thickness is determined by a balance of diffusion and settling velocity, as captured by the Péclet number Pe. As discussed earlier, this assumption is a relatively crude approximation, as one-way and two-way coupling effects can either delay or accelerate the particle settling. Hence, in principle, the concentration boundary layer can be thicker or thinner than the velocity boundary layer. However, the assumption of different boundary-layer thicknesses formally does not satisfy (2.29), and so our base state represents an approximate model rather than an exact solution of the full Navier–Stokes equations. It offers the advantage of clearly identifying the role of the dimensionless parameters, which will facilitate the physical interpretation later. We note that the assumption of 'model' base flows that do not represent exact solutions of the governing equations represents a common, well-established approach in linear stability theory. As an alternative, we could have obtained the base state by solving the governing equations numerically. This approach

would yield a quantitatively more accurate base state, at the expense of making it less straightforward to identify the role of the dimensionless parameters.

2.4. *Linearization and numerical implementation*

Each of the flow variables is decomposed into base flow and perturbation components, e.g. $u(y,z,t)=u_o(z)+u'(y,z,t)$, which are then substituted into (2.16)–(2.21). Subtracting the base flow and neglecting nonlinear perturbation terms yield a set of linear equations governing the evolution of the perturbations. For the field equations, this process is straightforward. For the interface equation we obtain

$$\frac{\partial \eta'}{\partial t}=\frac{c_\infty}{Pe}\left(c'(z=0)+\eta'\left.\frac{\mathrm{d}c_o}{\mathrm{d}z}\right|_{z=0}\right)-N\left(\left.\frac{\partial u'}{\partial z}\right|_{z=0}+\eta'\left.\frac{\mathrm{d}^2u_o}{\mathrm{d}z^2}\right|_{z=0}\right). \tag{2.41}$$

We assume normal mode perturbations that are periodic in y and grow exponentially in time, i.e. of the form

$$u'(y,z,t)=U(z)\sin(\alpha y)\mathrm{e}^{\sigma t}, \tag{2.42}$$
$$v'(y,z,t)=V(z)\cos(\alpha y)\mathrm{e}^{\sigma t}, \tag{2.43}$$
$$w'(y,z,t)=W(z)\sin(\alpha y)\mathrm{e}^{\sigma t}, \tag{2.44}$$
$$c'(y,z,t)=C(z)\sin(\alpha y)\mathrm{e}^{\sigma t}, \tag{2.45}$$
$$p'(y,z,t)=P(z)\sin(\alpha y)\mathrm{e}^{\sigma t}, \tag{2.46}$$
$$\eta'(y,t)=E\sin(\alpha y)\mathrm{e}^{\sigma t}. \tag{2.47}$$

Here, α denotes the spatial wavenumber of the perturbation, while σ represents its exponential growth rate. Capital letters indicate the perturbation eigenfunctions. The ansatz for the perturbations is in line with our goal to obtain insight into the formation of straight longitudinal channels. Clearly, there is the possibility that such channels may develop a streamwise structure, e.g. through meandering. The mechanisms behind such features would have to be explored via a secondary instability analysis, which is beyond the scope of the present investigation. Incorporating this perturbation ansatz into the linearized equations yields the following system of equations:

$$-\alpha V+\frac{\mathrm{d}W}{\mathrm{d}z}=0, \tag{2.48}$$
$$\sigma U+W\frac{\mathrm{d}u_o}{\mathrm{d}z}=\frac{1}{Re}\left(-\alpha^2U+\frac{\mathrm{d}^2U}{\mathrm{d}z^2}\right), \tag{2.49}$$
$$\sigma V=-\alpha P+\frac{1}{Re}\left(-\alpha^2V+\frac{\mathrm{d}^2V}{\mathrm{d}z^2}\right), \tag{2.50}$$
$$\sigma W=-\frac{\mathrm{d}P}{\mathrm{d}z}+\frac{1}{Re}\left(-\alpha^2W+\frac{\mathrm{d}^2W}{\mathrm{d}z^2}\right)-GC, \tag{2.51}$$
$$\sigma C+W\frac{\mathrm{d}c_o}{\mathrm{d}z}-\frac{1}{Pe}\frac{\mathrm{d}C}{\mathrm{d}z}=\frac{1}{Pe}\left(-\alpha^2C+\frac{\mathrm{d}^2C}{\mathrm{d}z^2}\right), \tag{2.52}$$
$$\sigma E=E\frac{c_\infty}{Pe}\left.\frac{\mathrm{d}c_o}{\mathrm{d}z}\right|_{z=0}-EN\left.\frac{\mathrm{d}^2u_o}{\mathrm{d}z^2}\right|_{z=0}+\frac{c_\infty}{Pe}C(z=0)-N\left.\frac{\mathrm{d}U}{\mathrm{d}z}\right|_{z=0} \tag{2.53}$$

with boundary conditions

$$U(z=0) + E\left.\frac{\mathrm{d}u_o}{\mathrm{d}z}\right|_{z=0} = 0, \tag{2.54}$$

$$V(z=0) = 0, \tag{2.55}$$

$$W(z=0) = \sigma E, \tag{2.56}$$

$$E\left.\frac{\mathrm{d}^2 c_o}{\mathrm{d}z^2}\right|_{z=0} + \left.\frac{\mathrm{d}C}{\mathrm{d}z}\right|_{z=0} = -\frac{NPe}{c_\infty}\left(E\left.\frac{\mathrm{d}^2 u_o}{\mathrm{d}z^2}\right|_{z=0} + \left.\frac{\mathrm{d}U}{\mathrm{d}z}\right|_{z=0}\right), \tag{2.57}$$

$$U(z\to\infty) = V(z\to\infty) = W(z\to\infty) = C(z\to\infty) = 0. \tag{2.58}$$

Equations (2.48)–(2.53) combined with the boundary conditions (2.54)–(2.58) comprise an eigenvalue problem of the form

$$\boldsymbol{A}\begin{pmatrix} U \\ V \\ W \\ C \\ E \\ P \end{pmatrix} = \sigma \boldsymbol{B}\begin{pmatrix} U \\ V \\ W \\ C \\ E \\ P \end{pmatrix}, \tag{2.59}$$

where the matrices $\boldsymbol{A}$ and $\boldsymbol{B}$ are given by

$$\boldsymbol{A} = \begin{pmatrix} \boldsymbol{M}_1 & \boldsymbol{0} & -\mathbf{d}_z u_o & \boldsymbol{0} & \boldsymbol{0} & \boldsymbol{0} \\ \boldsymbol{0} & \boldsymbol{M}_1 & \boldsymbol{0} & \boldsymbol{0} & \boldsymbol{0} & -\alpha \boldsymbol{I} \\ \boldsymbol{0} & \boldsymbol{0} & \boldsymbol{M}_1 & -G\boldsymbol{I} & \boldsymbol{0} & -\mathbf{d}_z \\ \boldsymbol{0} & \boldsymbol{0} & -\mathbf{d}_z c_o & \boldsymbol{M}_2 & \boldsymbol{0} & \boldsymbol{0} \\ M_3 & \boldsymbol{0} & \boldsymbol{0} & M_4 & M_5 & \boldsymbol{0} \\ \boldsymbol{0} & -\alpha \boldsymbol{I} & \mathbf{d}_z & \boldsymbol{0} & \boldsymbol{0} & \boldsymbol{0} \end{pmatrix}, \tag{2.60}$$

$$\boldsymbol{B} = \begin{pmatrix} \boldsymbol{I} & \boldsymbol{0} & \boldsymbol{0} & \boldsymbol{0} & \boldsymbol{0} & \boldsymbol{0} \\ \boldsymbol{0} & \boldsymbol{I} & \boldsymbol{0} & \boldsymbol{0} & \boldsymbol{0} & \boldsymbol{0} \\ \boldsymbol{0} & \boldsymbol{0} & \boldsymbol{I} & \boldsymbol{0} & \boldsymbol{0} & \boldsymbol{0} \\ \boldsymbol{0} & \boldsymbol{0} & \boldsymbol{0} & \boldsymbol{I} & \boldsymbol{0} & \boldsymbol{0} \\ 0 & 0 & 0 & 0 & 1 & 0 \\ \boldsymbol{0} & \boldsymbol{0} & \boldsymbol{0} & \boldsymbol{0} & \boldsymbol{0} & \boldsymbol{0} \end{pmatrix}, \tag{2.61}$$

with

$$\boldsymbol{M}_1 = \frac{1}{Re}[-\alpha^2 \boldsymbol{I} + \mathbf{d}_{zz}], \tag{2.62}$$

$$\boldsymbol{M}_2 = \frac{1}{Pe}[-\alpha^2 \boldsymbol{I} + \mathbf{d}_z + \mathbf{d}_{zz}], \tag{2.63}$$

$$M_3 = -N\mathrm{d}_z|_{z=0}, \tag{2.64}$$

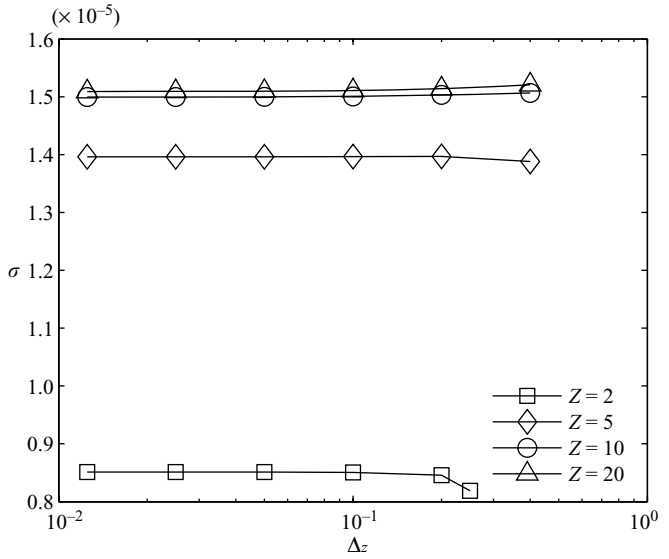

FIGURE 3. Convergence tests for the growth rate as a function of the domain size Z and the average grid spacing Δz. Parameters for this computation were $\alpha = 0.2$, $Re = Pe = 1000$, $L = 0.5$, $G = 10^{-1}$, $c_\infty = 10^{-2}$ and $N = 10^{-5}$.

$$M_4 = \frac{c_\infty}{Pe}, \tag{2.65}$$

$$M_5 = \frac{N}{L}\left(\frac{1}{L} - 1\right), \tag{2.66}$$

with the eigenvalue σ as the growth rate. The derivative operators in the z-direction ($\mathbf{d}_z$, $\mathbf{d}_{zz}$) are discretized by a second-order finite differencing scheme, with variable grid spacing to provide finer resolution close to the interface. The grid is generated using the hyperbolic tangent stretching method described in Fletcher (1991). The resulting eigensystem is solved by using the sparse eigensolver in MATLAB, which is based on LAPACK routines. The computational domain $0 \leqslant z \leqslant Z$ is discretized into N_z intervals. The value of Z needs to be sufficiently large, and the average grid spacing $\Delta z = Z/N_z$ sufficiently fine, for the solution to be independent of Z and N_z. Figure 3 provides relevant convergence information for a representative test case. Most calculations were performed for a domain height $Z = 20$ and $\Delta z = 2 \times 10^{-2}$.

3. Results

In this section, we discuss solutions to the eigenvalue problem (2.59) that provide $\sigma = \sigma(\alpha, Re, Pe, L, G, c_\infty, N)$. As usual, positive growth rates indicate perturbation modes that are unstable and grow exponentially in time, while negative growth rates are associated with damped modes. In general, we will keep Re and Pe equal, as the turbulent diffusion of momentum and particle concentration is assumed to occur with equal vigor.

Figure 4 depicts a representative family of dispersion relations for different $Re = Pe$. In this figure, as well as in corresponding figures presented later, only the largest eigenvalue is shown. For small wavenumbers, σ is seen to increase with α until it eventually reaches a maximum. Thereafter, it quickly decays and eventually becomes

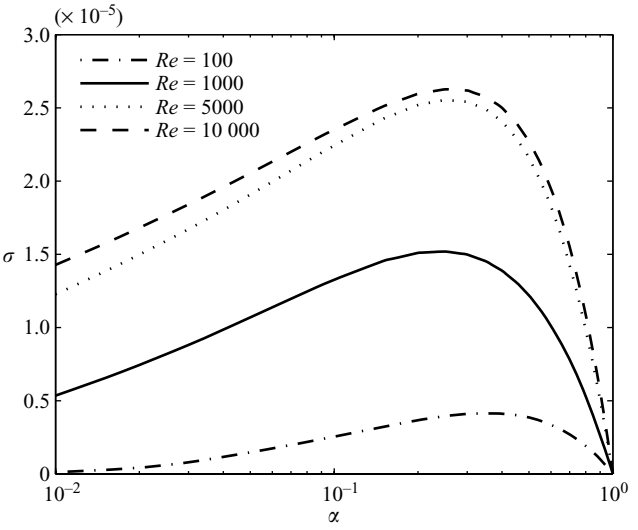

FIGURE 4. Representative dispersion relations for various values of $Pe = Re$, with $L = 0.5$, $G = 10^{-1}$, $c_\infty = 10^{-2}$ and $N = 10^{-5}$. Note that for all values of the Reynolds and Péclet numbers, the most dangerous wavenumber α_{max} is near 0.25. Furthermore, all dispersion relations display a cut-off wavenumber $\alpha_c = 1$.

negative. We refer to the wavenumber α_{max} associated with the highest growth rate σ_{max} as the most dangerous wave number. For a small amplitude, random initial perturbation α_{max} can be expected to become dominant in the sense that it will quickly overcome all other modes because of the exponential nature of perturbation growth. A critical Reynolds number does not appear to exist, as our calculations yield positive growth rates even for relatively small values of $Re = O(100)$. All of the dispersion relations exhibit a maximum growth rate for $\alpha_{max} \approx 0.25$. This indicates a dominant wavelength $\lambda_{max} = 2\pi/\alpha_{max}$ of $O(25)$, which is much larger than both the concentration and velocity boundary-layer thicknesses.

In order to gain insight into the physical mechanisms responsible for the instability, it is instructive to discuss the contributions of the individual terms in (2.53). A term-by-term examination of this equation sheds light on the mechanisms that govern the growth of interface perturbations. The first two terms on the right-hand side capture the effects of the perturbed interface location in the base concentration and velocity fields, while the last two terms describe the influence of the perturbation concentration and velocity fields. By differentiating the base flow profiles (2.39) and (2.40), and evaluating them at $z = 0$, we obtain

$$\frac{c_\infty}{Pe}\left.\frac{\mathrm{d}c_o}{\mathrm{d}z}\right|_{z=0} - N\left.\frac{\mathrm{d}^2 u_o}{\mathrm{d}z^2}\right|_{z=0} = \frac{N}{L}\left(\frac{1}{L} - 1\right). \tag{3.1}$$

Employing this simplification in (2.53), we obtain

$$\sigma = \frac{N}{L}\left(\frac{1}{L} - 1\right) + \frac{c_\infty}{PeE}C(z=0) - \frac{N}{E}\left.\frac{\mathrm{d}U}{\mathrm{d}z}\right|_{z=0}. \tag{3.2}$$

Positive terms on the right-hand side supply a destabilizing mechanism, while negative terms act in a stabilizing fashion. The first term on the right-hand side of (3.2) primarily reflects the influence of L, i.e. the ratio of the thicknesses of the base

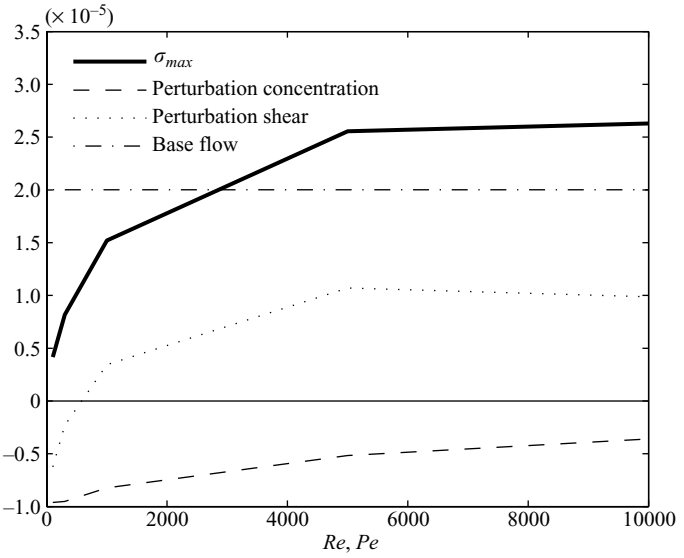

FIGURE 5. Maximum growth rate as a function of Re and Pe, for $L = 0.5$, $G = 10^{-1}$, $c_\infty = 10^{-2}$ and $N = 10^{-5}$. The solid line shows the dependence of σ_{max} on Re and Pe. Increasing Re and Pe has a uniformly destabilizing effect on the system. The contributions from the individual terms on the right-hand side of (3.2) to the overall growth rate are also shown.

velocity and concentration profiles. For $L < 1$ the term is positive, and so it contributes to the instability. Physically, $L < 1$ indicates that the base profile of the suspended particle concentration is thicker, i.e. decays more slowly, than its velocity counterpart. This implies that as an interface bump intrudes into the flow, it finds itself in an environment where particle settling decreases more slowly than erosion due to the shear stress, which will amplify the initial protrusion. Conversely, a local valley in the sediment bed will see erosion increase more strongly than sedimentation, which again will amplify the initial perturbation. This existence of a base flow velocity boundary layer that is thinner than the base concentration profile represents the main mechanism driving the channelization instability. We can thus identify $L < 1$ as the key criterion for instability to occur.

For $L > 1$, on the other hand, the velocity boundary layer is thicker than the concentration boundary layer. As an interface perturbation intrudes into the flow, particle settling diminishes faster than shear-induced erosion, which will dampen the original perturbation. A valley in the sediment bed will see settling increase more rapidly than erosion, which again will inhibit further growth of the perturbation. For $L = 1$ there is no direct effect of the base flow on the interfacial stability. The identification of L as the key stability parameter for channelization emerges as the main finding from the present analysis. Note that this result relies crucially on the fact that the analysis resolves the vertical structure of the current. A depth-averaged approach could not arrive at this result.

The last two terms on the right-hand side of (3.2) describe the influence of the concentration perturbation C and the perturbation shear $\mathrm{d}U/\mathrm{d}z$ on the interfacial stability. Figure 5 indicates that the C-term is always stabilizing, while the $\mathrm{d}U/\mathrm{d}z$-term is stabilizing for small values of $Re = Pe$ and destabilizing for larger values.

In order to understand the role of these terms in amplifying or damping the instability, it is helpful to analyse the structure of the eigenfunctions. Towards this

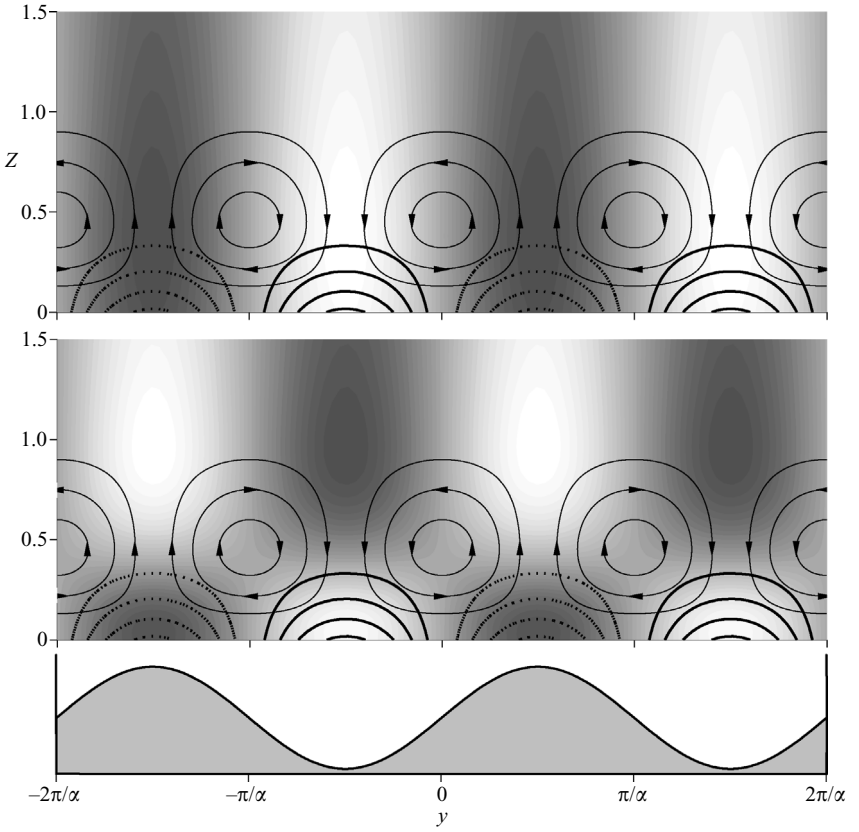

FIGURE 6. Dominant unstable eigenfunction modes for $\alpha_{max} = 0.24$, $Re = Pe = 1000$, $L = 0.5$, $G = 10^{-1}$, $c_\infty = 10^{-2}$ and $N = 10^{-5}$. The solid and dashed lines depict positive and negative concentration perturbation contours, respectively. Streamlines of the transverse perturbation velocity field are superimposed, with arrows denoting the flow direction. In the top frame, grey shading reflects the perturbation u-velocity, with lighter areas indicating positive values and darker areas negative values. The middle frame shows perturbation shear $\partial u/\partial z$ through grey shading, with lighter areas indicating positive values and darker areas negative values. The shape of the interface perturbation is shown in the bottom frame.

end, figure 6 shows the interfacial shape, along with the concentration disturbance and the streamwise and transverse perturbation velocity fields in the y, z-plane, for the representative case of $\alpha_{max} = 0.24$ and $Re = Pe = 1000$. All other parameter values are as in figure 4. The shape of the interface perturbation is shown in the bottom frame. The semicircular lines close to the interface in the top and middle frames represent concentration perturbation contours, with solid lines indicating positive values and dashed lines negative values. Streamlines of the transverse velocity perturbations are superimposed, with arrows denoting the direction of the flow. In the top frame, grey shading reflects the perturbation u-velocity, with lighter areas indicating positive values and darker areas negative values. Above the peaks of the perturbed interface, we observe a negative concentration perturbation (reduced particle loading), which results in lower hydrostatic pressure as compared to the troughs of the interface, where the particle concentration increases. Hence a spanwise pressure gradient exists along the interface, which drives a perturbation flow from the troughs to the peaks. Via the continuity equation, this perturbation flow along the interface leads to the formation

of the counter-rotating streamwise vortices visible in the figure. Note that above the peaks, these vortices carry low-speed fluid, i.e. fluid with a small streamwise velocity, away from the interface, while high-speed fluid from the free stream is brought towards the interface at the troughs. In this way the shear stress, which primarily is a function of the local streamwise velocity gradient, is enhanced above the troughs and lowered above the peaks. This is reflected by the middle frame of the figure, which shows the perturbation shear $\partial u/\partial z$ through grey shading, with lighter areas indicating positive values and darker areas negative values. Thus, in turn, erosion increases in the valleys and decreases at the peaks, which further amplifies the initial concentration perturbation.

Note that the vertical extent of the velocity and concentration eigenfunctions is limited to the near-wall region, where the base velocity increases and the sediment concentration decreases. This indicates that the detailed features of the base flow far away from the sediment bed do not have an appreciable influence on the instability, which justifies a posteriori our assumption of boundary conditions (2.33) and (2.35) for the base flow.

On the basis of these eigenfunction structures, we can now understand the role of the second term on the right-hand side of (3.2), which reflects the rate of particle settling at the interface as a result of the perturbation concentration. This effect is destabilizing if C and E are of the same sign, i.e. if the concentration perturbation is positive above the peaks of the interface. Figure 5 and the eigenfunction plot in figure 6 indicate that for this representative case C and E are of opposite signs, and so the effect of settling as a result of the concentration perturbation field is stabilizing.

The third term on the right-hand side of (3.2) accounts for the rate at which particle volume is removed from the interface as a result of the shear stress induced by the velocity perturbation U. Figure 5 indicates that for the representative case discussed earlier, this effect is destabilizing, which indicates that E and $\mathrm{d}U/\mathrm{d}z$ must be of opposite signs. This confirms the physical picture developed on the basis of figure 6, in that the perturbation shear stress $\partial u/\partial z$ is negative at interfacial peaks and positive in troughs. The erosion of particles decreases and increases, respectively.

Hence, the case shown in figure 6 depicts a situation for which the secondary transverse flow and the shear stress it causes are destabilizing (cf. figure 5). For smaller values of Re and Pe, on the other hand, this figure shows the perturbation shear to be stabilizing. An inspection of the corresponding eigenfunctions (not shown) indicates that for such a case the streamwise vortices rotate in the opposite direction.

Figure 7 shows the contributions of the individual terms in (3.2) to the overall dispersion relation. The base flow term is independent of the eigenfunctions and hence contributes a constant value for all wavenumbers. Interestingly at the cutoff wavenumber, where the overall growth rate is zero, the concentration perturbation vanishes, and the destabilizing contribution of the base flow term is balanced by the stabilizing perturbation shear term. The reason for this can be found in the governing equations. For $C \equiv 0$, boundary condition (2.57) yields

$$\frac{1}{E}\frac{\mathrm{d}U}{\mathrm{d}z}\bigg|_{z=0} = \frac{1}{L^2} - \frac{1}{L}. \tag{3.3}$$

By substituting (3.3) into (3.2), we immediately obtain that $\sigma = 0$ when $C \equiv 0$. For $C \equiv 0$, (2.52) furthermore states that $W \equiv 0$. For $\sigma = 0$, (2.49) then yields

$$\frac{\mathrm{d}^2U}{\mathrm{d}z^2} - \alpha_c^2 U = 0, \tag{3.4}$$

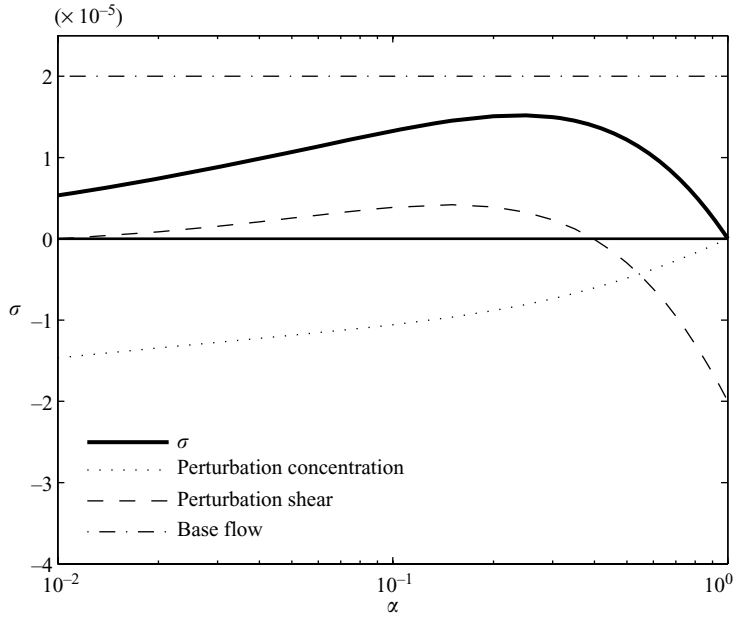

FIGURE 7. The overall dispersion relation for $Pe = Re = 1000$, $L = 0.5$, $G = 10^{-1}$, $c_\infty = 10^{-2}$ and $N = 10^{-5}$, along with the contributions of the individual terms in (3.2).

which, together with the boundary conditions for U, leads to

$$U(z) = -\frac{E}{L} e^{-\alpha_c z}. \tag{3.5}$$

Substitution into (3.3) immediately yields for the cutoff wavenumber

$$\alpha_c = \frac{1}{L} - 1. \tag{3.6}$$

For $L = 0.5$, we obtain $\alpha_c = 1$, in agreement with figures 4 and 7.

Figure 8 displays dispersion relations for $0.1 \leqslant L \leqslant 0.9$. As L increases, both the maximum growth rate σ_{max} and the associated wavenumber α_{max} decrease, until eventually for $L = 1$ the system becomes stable to perturbations of all wavenumbers. For $L < 0.5$, the scaled maximum growth rate becomes independent of L, indicating that the growth is dominated by the base flow term.

3.1. *Influence of the gravitational parameter G*

As we vary G over three orders of magnitude, the growth rate increases only by a factor of approximately 5, while the dominant wavenumber remains roughly constant (cf. figure 9). An inspection of the system of governing equations suggests that G primarily affects the secondary transverse flow via (2.51). Hence the counter-rotating streamwise vortices will grow stronger as G increases. This is confirmed by figure 10 which shows an increase in the destabilizing effect of the perturbation shear as G increases. Note that our finding of a destabilizing effect of G is in contrast to the observations by Colombini (1993), who found gravity to have a stabilizing effect. This difference can be traced back to the consideration of bedload only in the work of Colombini (1993), which shows that gravity has the effect of moving sediment from the peaks to the valleys. On the other hand, in the present formulation a

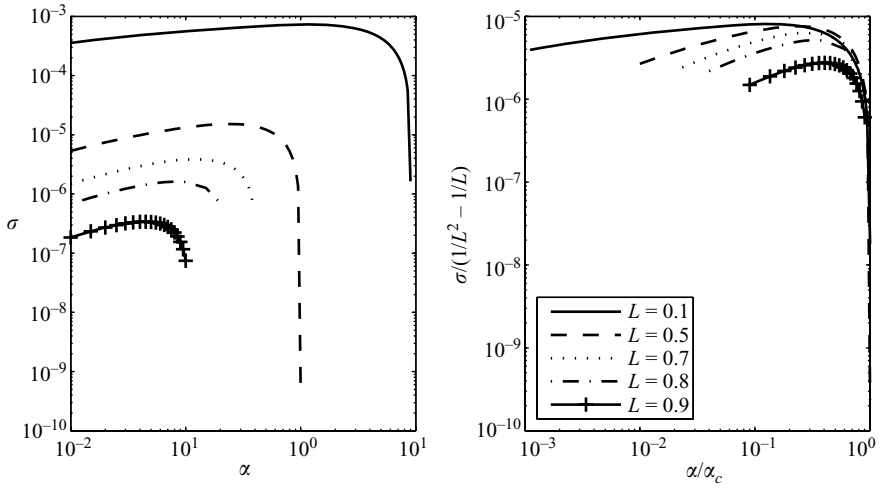

FIGURE 8. Dispersion relations for various values of L, along with $Re = Pe = 1000$, $G = 10^{-1}$, $c_\infty = 10^{-2}$ and $N = 10^{-5}$. (a) Unscaled results; (b) σ scaled with the base flow contribution $(1/L^2 - 1/L)$ and α scaled with the cut-off wavenumber $(1/L - 1)$.

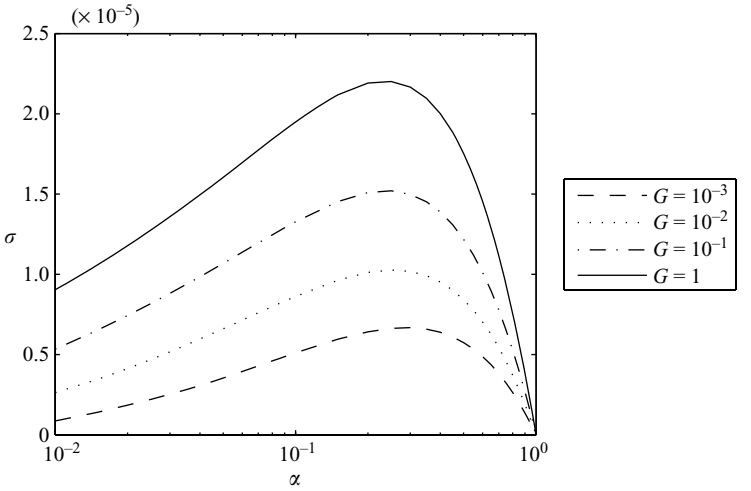

FIGURE 9. Dispersion relations for various values of the gravitational parameter G, along with $Re = Pe = 1000$, $L = 0.5$, $c_\infty = 10^{-2}$ and $N = 10^{-5}$. A variation of G over three orders of magnitude results only in a modest increase of the growth rate, which indicates that the base flow term, which is independent of G, dominates the perturbation growth.

larger gravitational term will strengthen the secondary streamwise vortices, thereby accelerating the growth of the instability.

3.2. *Influence of the sediment loading parameter* c_∞/Pe

The parameter c_∞ represents the free stream volume fraction of suspended particles. c_∞/Pe then is the volume flux of sedimenting particles far from the sediment bed. When multiplied by the dimensionless concentration at the interface, it gives the rate at which particle volume accumulates at the interface due to settling. Note that c_∞/Pe appears only in (2.53), which governs the evolution of the interface, and in boundary

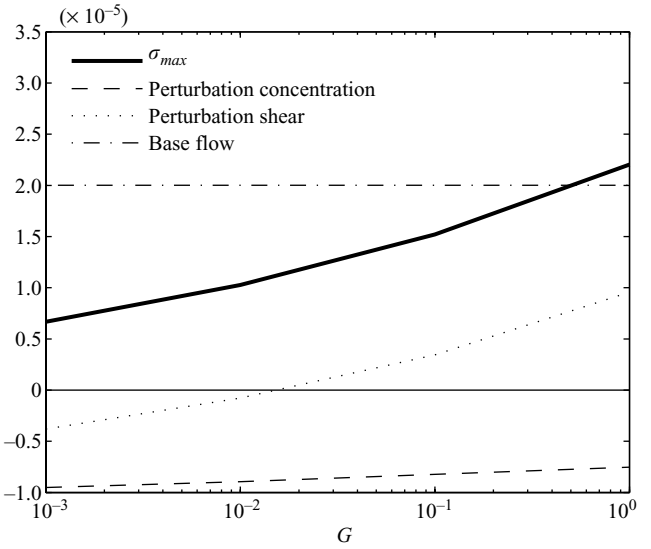

FIGURE 10. Individual contributions to the maximum growth rate as functions of the gravitational parameter G, for $Re = Pe = 1000$, $L = 0.5$, $c_\infty = 10^{-2}$ and $N = 10^{-5}$. An increase in G is seen to amplify the secondary streamwise vortices, and hence the perturbation shear, thereby strengthening the instability.

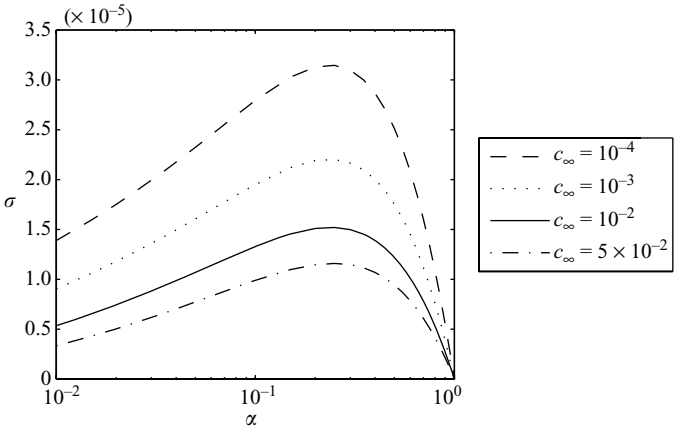

FIGURE 11. Dispersion relations for various values of the sediment loading parameter c_∞, along with $Re = Pe = 1000$, $L = 0.5$, $G = 10^{-1}$ and $N = 10^{-5}$. While increased particle loading is seen to have a stabilizing effect, the most dangerous wavenumber depends only weakly on c_∞.

condition (2.57), which links the resuspension flux to the local shear stress. Figure 11 displays dispersion relations for c_∞ ranging from 10^{-4} to 5×10^{-2}. Increased particle loading is seen to have a stabilizing influence on the interface. The cutoff wavenumber is independent of c_∞, while the dominant wavenumber α_{max} shows a weak dependence on the sediment loading parameter.

Figure 12 shows the maximum growth rate σ_{max} as a function of c_∞, along with the individual contributions from the terms in (3.2). Interestingly, the stabilizing effect due to the perturbation concentration term involving $C(z)$ in (3.2) increases only slightly

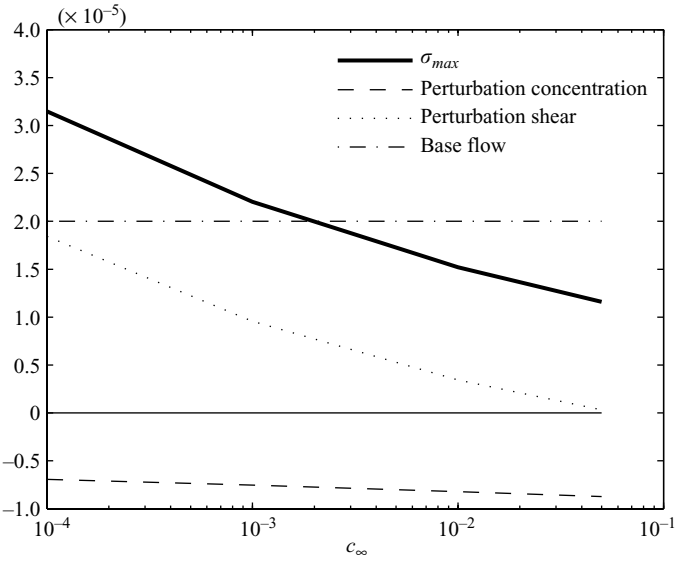

FIGURE 12. Individual contributions to the maximum growth rate as functions of the settling loading parameter c_∞, along with $Re = Pe = 1000$, $L = 0.5$, $G = 10^{-1}$ and $N = 10^{-5}$. For larger sediment loading parameters, the destabilizing contribution of the perturbation shear stress diminishes.

with c_∞, even though it is this term that contains c_∞/Pe. The figure indicates that the influence of increasing c_∞/Pe is primarily felt in a reduction of the destabilizing effect of perturbation shear. The reason for this lies in the way in which the process of non-dimensionalization affects the base concentration profile (cf. (2.40)). For a larger value of c_∞, the process of rendering the governing equations dimensionless will lead to a smaller gradient $\mathrm{d}c_o/\mathrm{d}z$ of the dimensionless base concentration profile at the interface. Hence, for a larger c_∞ an interfacial dislocation will result in a weaker dimensionless concentration perturbation, and hence in weaker streamwise vortices. Consequently, the vertical transport of low- and high-speed fluid above the interfacial peaks and troughs is reduced, and the destabilizing perturbation shear decreases.

3.3. *Influence of the erosion parameter N*

The erosion parameter N quantifies the dimensionless rate at which particle volume is removed from the substrate per unit shear. Larger values of N imply that it is relatively easier for the particles to be re-entrained into the flow. Primarily, this parameter affects the base flow term on the right-hand side of (3.2), amplifying the stabilizing or destabilizing effect of L discussed earlier. In addition, it multiplies the perturbation shear term in (3.2). Figure 13 shows dispersion relations obtained for $10^{-6} \leqslant N \leqslant 10^{-4}$. After scaling the growth rate with N, the dispersion relations nearly collapse. This indicates that the base flow and perturbation shear terms in (3.2), both of which are proportional to N, dominate the growth rate, while the perturbation settling term remains small over the range of N considered.

4. Discussion and conclusions

The current investigation analyses the linear stability of an erodible sediment bed beneath a turbidity current with regard to spanwise perturbations, in order to

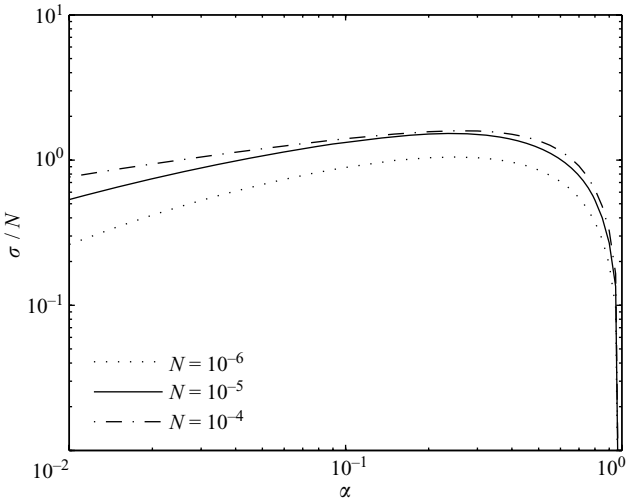

FIGURE 13. Dispersion relations for various values of the erosion parameter N, along with $Re = Pe = 1000$, $L = 0.5$, $G = 10^{-1}$ and $c_\infty = 10^{-2}$. When scaling the growth rate with N, the dispersion relations nearly collapse, indicating that the base flow and the perturbation shear term dominate over the perturbation settling term.

identify potential mechanisms responsible for the formation of longitudinal gullies and channels. To our knowledge, it represents the first attempt at a formal stability analysis that accounts for the coupled interaction of the three-dimensional fluid and suspended sediment motion with the erodible bed below.

As the main criterion for instability, the analysis yields that $L < 1$. Physically, this implies that for instability to occur, the suspended sediment concentration needs to decay more slowly away from the sediment bed than the shear stress. Under such conditions, an upward protrusion of the surface of the sediment bed will find itself in an environment where erosion decays more quickly than sedimentation, and so it will keep growing. Conversely, a local valley in the sediment bed will see erosion increase more strongly than sedimentation, which again will amplify the initial perturbation. Note that the derivation of this stability criterion requires an approach that resolves the vertical velocity and concentration structure of the current. It could not have been obtained from an analysis based on a set of depth-averaged equations.

Laboratory experiments provide evidence that turbidity currents frequently do give rise to $L < 1$, and so the instability mechanism identified here is relevant. For example, the measurements reported by Parker *et al.* (1987), Garcia (1994), Altinakar *et al.* (1996), McCaffrey *et al.* (2003) and Choux *et al.* (2005) show that the concentration of suspended sediment decays over a length scale comparable to the height of the current (see also Normark 1989), whereas the streamwise velocity profile reaches a maximum at substantially less than half the current height (typically 0.2–0.3; Kneller & Buckee 2000) and subsequently decays (see also Stacey & Bowen 1988). This would indicate a value of L on the order of one half.

The destabilizing effect of the base flow for $L < 1$ is modulated by the perturbation of the suspended sediment concentration, and by the perturbation shear stress due to a secondary flow structure in the form of counter-rotating streamwise vortices. While the perturbation concentration is uniformly stabilizing, the streamwise vortices are stabilizing for small Reynolds and Péclet numbers and destabilizing for large values.

Since we do not know the precise form of the turbulent stress tensor in a complex flow such as the present one, we employ the simplest possible turbulence model in the form of a constant eddy viscosity. The analysis shows that this approach is adequate for capturing the basic instability mechanism.

It is of interest to compare the present approach to the earlier linear stability analysis by Colombini (1993), who considered the effect of a secondary flow structure on the spanwise bedload transport. He found the sediment bed stability to be governed by a balance of the destabilizing secondary flow and the stabilizing effects of gravity. Our current approach, on the other hand, considers the effect of suspended sediment on the flow, with secondary streamwise vortices emerging naturally. While the investigation by Colombini (1993) identifies the streamwise vortices as the main ingredient driving the instability, our analysis shows the main cause for the instability to be the difference in concentration and velocity boundary-layer thicknesses. The streamwise vortices can be stabilizing or destabilizing depending on the parameter regime.

An interesting related analysis is given by Thorsness & Hanratty (1979), although for a quite different type of flow (cf. also the review by Hanratty 1981). These authors consider the emergence of streamwise waves in dissolving or depositing solid surfaces such as cave walls or river ice. For these streamwise waves, the phase difference between the surface deformation and the mass transfer rate determines the stability properties and the propagation direction of the waves.

The present linear stability analysis provides the most amplified wavelength of about 25 times the height over which the suspended sediment concentration decays. For representative current heights of 10–100 m, this yields gully spacings of about 250–2500 m, which are consistent with the observations by Greene, Maher & Paull (2002) (500–2000 m) as well as by McAdoo, Pratson & Orange (2000) and Driscoll, Weissel & Goff (2000) (a few hundred metres to a few kilometres). It is to be kept in mind that currents at the upper end of this range of magnitudes may behave differently in some aspects from the laboratory-scale currents employed to study sediment erosion (Garcia & Parker 1993). Nevertheless, it is interesting that the present analysis yields gully spacings consistent with field observations. This spacing is in the same range as the linear stability results by Izumi (2004) (150–8000 m). On the other hand, field observations by Field *et al.* (1999) report channel spacings of 180–1000 m. Note, however, that the most amplified wavenumber is largely insensitive to the values of Re, Pe, G and c_∞, and so the preferred wavelength is roughly proportional to the turbidity current height. Hence, currents with a height somewhat smaller than 100 m may well be able to produce spacings in the range observed by Field *et al.* (1999). We remark that it might be difficult to reproduce these observations in laboratory-scale facilities. Even for a relatively small current height of 10 cm, the predicted spanwise wavelength would be on the order of 2.5 m, which exceeds the size of most flumes.

In contrast to previous analyses based on various systems of depth-averaged equations, the instability mechanism identified in the present analysis does not require any assumptions about sub- or supercritical flow. Furthermore, it does not require the presence of a slope break, a curved slope or, for that matter, a slope at all. However, field observations indicate that such topographical features may promote the formation of gullies and channels. Hence it would be interesting to investigate the extent to which slope breaks, curved slopes or sub- and supercritical currents may play a role in generating flows for which $L < 1$. Two-dimensional nonlinear simulations based on the Navier–Stokes equations should be able to provide information in this regard.

The analysis furthermore sheds light on the influence of additional dimensionless parameters, viz. Re, Pe, G, c_∞ and N. An increase in Re and Pe increases the growth rate, as it enhances the destabilizing effect of the counter-rotating streamwise vortices. For the same reason, an increase in the gravitational parameter G is destabilizing as well. On the other hand, increasing the sediment loading parameter c_∞ has a stabilizing influence. The erosion parameter N is seen to have a weak overall influence.

Clearly, some of the assumptions invoked here represent idealizations of real flows. For example, the current analysis is based on the Boussinesq equations, implying that any density variations due to particle loading are relatively modest. Real flows, in contrast, may exhibit sufficiently high suspended sediment concentrations to give rise to non-Boussinesq effects (Birman, Martin & Meiburg 2005; Etienne, Hopfinger & Saramito 2005; Lowe, Rottman & Linden 2005). Similarly, such large concentrations can modify the effective viscosity of the suspension, and they can affect the sedimentation velocity due to hindered settling (Ham & Homsy 1988). However, while these effects may modify the results quantitatively to some degree, they are unrelated to the fundamental nature of the instability mechanism identified by the analysis. Similarly, we wish to point out that by focusing on the well-developed flow in a cross-section some distance behind the front of the current, the present analysis is unable to elucidate any potential connections between the formation of channels and the lobe and cleft instability at the current front (Simpson 1997; Härtel, Carlsson & Thunblom 2000; Härtel, Meiburg & Necker 2000).

Perhaps the most far-reaching approximation invoked in this analysis is the assumption of a linear relationship between the bed shear stress and the erosional particle flux rather than the more threshold-like behaviour reported by Garcia & Parker (1993). This threshold-like behaviour may limit the appearance of the sediment bed instability to certain flow regimes. For flows involving only very small shear stresses, the instability may be too weak to be noticeable. On the other hand, for very rapid flows that give rise to extremely large shear stresses, saturation may become important, and so the bed is eroded uniformly without noticeable spatial variations. However, in the important transitional regime where any increase in the bed shear stress translates into a higher erosional particle flux, the basic mechanism identified here will still be effective in giving rise to spatially periodic erosional patterns. In this context, it will be interesting to extend the current analysis by performing fully nonlinear simulations based on a threshold-like relationship between bed shear stress and erosion.

The authors gratefully acknowledge financial support from BHP Billiton Petroleum, as well as fruitful discussions with Bill McCaffrey, Michael Glinsky, Chris Lerch, Moshe Strauss and Rama Govindarajan.

REFERENCES

Altinakar, M. S., Graf, W. H. & Hopfinger, E. J. 1996 Flow structure in turbidity currents. *J. Hydraul. Res.* **34**, 713–718.

Birman, V. K., Martin, J. E. & Meiburg, E. 2005 The non-Boussinesq lock-exchange problem. Part 2. High-resolution simulations. *J. Fluid Mech.* **537**, 125–144.

Birnir, B., Smith, T. R. & Merchant, G. E. 2001 The scaling of fluvial landscapes. *Comput. Geosci.* **27**, 1217–1230.

Blanchette, F., Strauss, M., Meiburg, E., Kneller, B. & Glinsky, M. E. 2005 High resolution numerical simulations of resuspending gravity currents: conditions for self-sustainment. *J. Geophys. Res. C:* **110**, C12022, doi:10.1029/2005JC002927.

Bloneaux, P. 2001 Mechanics of coastal forms. *Annu. Rev. Fluid Mech.* **33**, 339–370.

Bosse, T., Kleiser, L. & Meiburg, E. 2006 Small particles in homogeneous turbulence: settling velocity enhancement by two-way coupling. *Phys. Fluids* **18**, 027102.

Campbell, D. C., Shimeld, J. W., Mosher, D. C. & Piper, D. J. W. 2004 Relationships between sediment mass failure modes and magnitudes in the evolution of the Scotian Slope, offshore Nova Scotia. In *Offshore Technology Conference, Houston, Texas, Paper 16743.*

Chikita, K. 1989 A field study of turbidity currents initiated by spring run-offs. *Water Resour. Res.* **25**, 257–271.

Chikita, K. 1990 Sedimentation by river-induced turbidity currents: field measurements and interpretation. *Sedimentology* **37**, 891–905.

Choux, C. M. A., Baas, J. H., McCaffrey, W. D. & Haughton, P. D. W. 2005 Comparison of spatio-temporal evolution of experimental particulate gravity flows at two different initial concentrations, based on velocity, grain size and density data. *Sedim. Geol.* **179**, 49–69.

Colombini, M. 1993 Turbulence-driven secondary flows and formation of sand ridges. *J. Fluid Mech.* **254**, 701–719.

Colombini. M. & Parker, G. 1995 Longitudinal streaks. *J. Fluid Mech.* **304**, 161–183.

Driscoll, N. W., Weissel, J. K. & Goff, J. A. 2000 Potential for large-scale submarine slope failure and tsunami generation along the U.S. mid-Atlantic coast. *Geology* **28**(5), 407–410.

Engelund, F. 1964 A practical approach to self-preserving turbulent flows. *Acta Polytechnica Scandinavica, Civil Engineering and Building Construction Series* **27**, 6.

Etienne, J., Hopfinger, E. J. & Saramito, P. 2005 Numerical simulations of high density ratio lock-exchange flows. *Phys. Fluids* **17**(3), 036601.

Fedele, J. J. 2003 Bedforms and gravity underflows in marine environments. PhD thesis, University of Illinois at Urbana-Champaign.

Field, M. E., Gardner, J. V. & Prior, D. B. 1999 Geometry and significance of stacked gullies on the northern California slope. *Mar. Geol.* **154**, 271–286.

Fletcher, C. 1991 *Computational Techniques for Fluid Dynamics 2*. Springer.

Garcia, M. H. 1994 Depositional turbidity currents laden with poorly sorted sediment. *J. Hydraul. Engng* **120**, 1240–1263.

Garcia, M. H. & Parker, G. 1993 Experiments on the entrainment of sediment into resuspension by a dense bottom current. *J. Geophys. Res.* **98**, 4793–4807.

Greene, H. G., Maher, M. & Paull, C. K. 2002 Physiography of the Monterey Bay National Marine Sanctuary and implications about continental margin development. *Mar. Geol.* **181**, 55–82.

Gyr, A. & Kinzelbach, W. 2004 Bed forms in turbulent channel flow. *Appl. Mech. Rev.* **57**(1), 77–93.

Ham, J. M. & Homsy, G. M. 1988 Hindered settling and hydrodynamic dispersion in quiescent sedimenting suspensions. *Intl J. Multiphase Flow* **14**(5), 533–546.

Hanratty, T. J. 1981 Stability of surfaces that are dissolving or being formed by convective diffusion. *Annu. Rev. Fluid Mech.* **13**, 231–252.

Härtel, C., Carlsson, F. & Thunblom, M. 2000 Analysis and direct numerical simulation of the flow at a gravity-current head. Part 2. The lobe-and-cleft instability. *J. Fluid Mech.* **418**, 213–229.

Härtel, C., Meiburg, E. & Necker, F. 2000 Analysis and direct numerical simulations of the flow at a gravity current head. Part 1. Flow topology and front speed for slip and no-slip boundaries. *J. Fluid Mech.* **418**, 189–212.

Imran, J., Parker, G. & Katopodes, N. 1998 A numerical model of channel inception on submarine fans. *J. Geophys. Res.* **103**, 1219–1238.

Izumi, N. 2004 The formation of submarine gullies by turbidity currents. *J. Geophys. Res.* **109**, C03048.

Izumi, N. & Fujii, K. 2006 Channelization on plateaus composed of weakly cohesive fine sediment. *J. Geophys. Res.* **111**, F01012, doi:10.1029/2005JF000345.

Izumi, N. & Parker, G. 1995 Inception of channelization and drainage basin formation: upstream-driven theory. *J. Fluid Mech.* **283**, 341–363.

Izumi, N. & Parker, G. 2000 Linear stability analysis of channel inception: downstream-driven theory. *J. Fluid Mech.* **419**, 239–262.

Kneller, B. C. & Buckee, C. M. 2000 The structure and fluid mechanics of turbidity currents; a review of some recent studies and their geological implications. *Sedimentology* **47**(Suppl. 1), 62–94.

Komar, P. D. 1969 The channelized flow of turbidity currents with application to Monterey deep-sea fan channel. *J. Geophys. Res.* **74**(18), 4544–4558.

Lowe, R. J., Rottman, J. W. & Linden, P. F. 2005 The non-Boussinesq lock-exchange problem. Part 1. Theory and experiments. *J. Fluid Mech.* **537**, 101–124.

McAdoo, B. G., Pratson, L. & Orange, D. L. 2000 Submarine landslide geomorphology, US continental slope. *Mar. Geol.* **169**, 103–136.

McCaffrey, W. D., Choux, C. M., Baas, J. H. & Haughton, P. D. W. 2003 Spatio-temporal evolution of velocity structure, concentration and grain-size stratification within experimental particulate gravity currents. *Mar. Petrol. Geol.* **20**, 851–860.

Necker, F., Härtel, C., Kleiser, L. & Meiburg, E. 2002 High-resolution simulations of particle-driven gravity currents. *Intl J. Multiphase Flow* **28**, 279–300.

Necker, F., Härtel, C., Kleiser, L. & Meiburg, E. 2005 Mixing and dissipation in particle-driven gravity currents. *J. Fluid Mech.* **545**, 339–372.

Normark, W. R. 1989 Observed parameters for turbidity-current flow in channels, Reserve Fan, Lake Superior. *J. Sedim. Petrol.* **59**, 423–431.

Parker, G. 1978 Self-formed straight rivers with equilibrium banks and mobile bed Part 1. The sand-silt river. *J. Fluid Mech.* **89**(1), 109–125.

Parker, G., Garcia, M., Fukushima, M. & Yu, W. 1987 Experiments on turbidity currents over an erodible bed. *J. Hydraul. Res.* **25**, 123–147.

Piper, D. J. W. & Savoye, B. 1993 Processes of late quaternary turbidity current flow and deposition on the Var deep-sea fan, north-west Mediterranean sea. *Sedimentology* **40**, 557–582.

Raju, N. & Meiburg, E. 1995 The accumulation and dispersion of heavy particles in forced two-dimensional mixing layers. II. The effect of gravity. *Phys. Fluids* **7**(6), 1241–64.

Revelli, R. & Ridolfi, L. 2000 Inception of channelization over a non-flat bed. *Meccanica* **35**, 457–461.

Simpson, J. E. 1997 *Gravity Currents in the Environment and the Laboratory*, 2nd edn. Cambridge University Press.

Smith, T. R. & Bretherton, F. P. 1972 Stability and the conservation of mass in drainage basin evolution. *Water Resour. Res.* **8**, 1506–1529.

Stacey, M. W. & Bowen, A. J. 1988 The vertical structure of density and turbidity currents: theory and observations. *J. Geophys. Res.* **93**, 3528–3542.

Syvitski, J., Field, M., Alexander, C., Orange, D., Gardner, J. & Lun, L. 1996 Continental-slope sedimentation: the view from northern California. *Oceanography* **9**, 163–167.

Thorsness, C. B. & Hanratty, T. J. 1979 Stability of dissolving or depositing surfaces. *AIChE J.* **25**(4), 697–701.

Wang, Z. & Cheng, N. 2005 Secondary flows over artificial bed strips. *Adv. Water Res.* **28**, 441–450.

Zeng, J., Lowe, D. R., Prior, D. B. & Wiseman Jr, W. D. 1991 Flow properties of turbidity currents in Bute Inlet, British Columbia. *Sedimentology* **38**, 975–996.